Journal of Materials Chemistry A

PAPER

View Article Online
View Journal | View Issue

Cite this: J. Mater. Chem. A, 2018, 6, 13816

A new 3D Dirac nodal-line semi-metallic graphene monolith for lithium ion battery anode materials†

Jie Liu, [a] Xiaoyin Li,[a] Qian Wang, *[a] Yoshiyuki Kawazoe[b] and Puru Jena[c]

Received 12th May 2018
Accepted 19th June 2018

DOI: 10.1039/c8ta04428g

rsc.li/materials-a

Due to the limited specific capacity of graphite, it is highly desirable to develop new alternatives for high performance lithium ion battery (LIB) anode materials. Motivated by the recent synthesis of three-dimensional (3D) graphene (*Phys. Rev. Lett.*, 2016, **116**, 055501), here we propose a new 3D graphene monolith, termed HZGM-42. State-of-the-art theoretical calculations uncover that HZGM-42 not only possesses high thermodynamic stability, anisotropic elasticity and high specific strength, but also exhibits a unique electronic band structure with Dirac nodal-lines. Equally important, HZGM-42 shows excellent electrical conductivity and uniformly distributed channels for the transport of Li ions with fast kinetics. As compared to the commercially used graphite anode, HZMG-42 possesses a much higher theoretical specific capacity (637.71 mA h g^{-1}), a much lower energy barrier (0.02 eV) for Li ion diffusion along the one-dimensional channels, and a much smaller volume change (2.4%) during charging and discharging operation. This study expands the family of 3D porous carbon materials with great potential for LIBs.

Introduction

Since the commercialization of lithium ion batteries (LIBs) in the early 1990s, graphite has been used as the standard anode material.[1] However, its limited specific capacity (372 mA h g^{-1}), significant volume change (10%), and poor cycling performance at high rates cannot meet the requirements for high-tech applications such as advanced electrical vehicles[2] and stationary energy storage.[3] Hence, anode materials with high storage capacity and high rate capability are highly desirable for next-generation LIBs. In the last three decades, tremendous effort has been devoted to the investigation of carbon materials for high-performance anodes in LIBs because of their unique advantages, such as availability, low cost, nontoxicity, and good lithium intercalation and de-intercalation reversibility.[4–7] Among various carbon anode materials, porous carbon is of particular interest[7–9] as the open pore structures can lead to a high specific surface area with a large amount of storage sites for Li-ions, which are favorable for high-capacity LIB anodes.[5,10] However, currently synthesized porous carbon materials[11–16] have some drawbacks when used as anode materials. Firstly, the conductivity of discovered porous carbon is relatively low. For instance, amorphous porous carbon[11] has low electrical conductivity due to its disordered pores and structural defects. Besides, it is difficult to control the arrangement and size of the pores during the synthesis of conventional porous carbon,[11–13] which is unfavorable for Li-ion transport, resulting in a low rate capability. Thus, a question arises: can we find a 3D carbon material with intrinsic ordered nano-pores as well as high electrical conductivity?

It is well known that graphene exhibits the best electrical conductivity among all of the carbon allotropes. Therefore, a possible way to construct a 3D porous carbon structure with high electrical conductivity is to assemble two-dimensional (2D) graphene sheets into 3D graphene monoliths. As a matter of fact, in recent years, many efforts have been made to achieve 3D graphene networks.[14–18] For instance, some 3D graphene monoliths have been synthesized by integrating zigzag-edged graphene nanoribbons.[19] These structures are found to possess intrinsic nanopores and the carrier velocity of electrons can reach $\sim 10^6$ m s^{-1},[20] indicating that these structures may have good potential as anode materials for LIBs. Inspired by these experimental studies, we propose a new 3D graphene monolith, named HZGM-42. We found that HZGM-42 possesses a suitable pore size for favorable Li adsorption, high electrical conductivity, well-organized channels for fast Li ion diffusion, and a small volume change during charging and discharging operation. These features are highly desirable for LIB anode materials. This work sheds light on the design of new materials with high capacity, rate capability and excellent stability for LIBs.

Computational methods

First-principles calculations were performed within the framework of density functional theory (DFT) implemented in the

[a]Center for Applied Physics and Technology, Department of Materials Science and Engineering, HEDPS, BKL-MEMD, College of Engineering, Peking University, Beijing 100871, China. E-mail: qianwang2@pku.edu.cn

[b]New Industry Creation Hatchery Center, Tohoku University, Sendai, 980-8577, Japan

[c]Department of Physics, Virginia Commonwealth University, Richmond, VA 23284, USA

† Electronic supplementary information (ESI) available. See DOI: 10.1039/c8ta04428g

Vienna *Ab initio* Simulation Package (VASP)[21] with the exchange–correlation functional in the Perdew–Burke–Ernzerhof (PBE) form.[22] The projector augmented wave (PAW) method[23] was used to treat the interactions between ion cores and valence electrons. The plane-wave cutoff energy for the wave function was set to 500 eV. The Heyd–Scuseria–Ernzerhof (HSE06) hybrid functional[24] was used for accurate calculations of the electronic structure. For geometry relaxations, the convergence thresholds were set to 10^{-4} eV and 10^{-3} eV Å^{-1} for total energy and force component, respectively. The first Brillouin zone was represented by k points sampled using the Monkhorst–Pack scheme[25] with a grid density of $2\pi \times 0.02$ Å^{-1}. *Ab initio* molecular dynamics (AIMD) simulations were performed using the canonical ensemble (NVT) with the Nosé thermostat[26] to examine thermal stability. The calculations of phonon dispersions were carried out by using the linear response method within the density functional perturbation theory[27] as implemented in the Phonopy code.[28] The diffusion barriers of Li ions were calculated by using the climbing-image nudged elastic band (CI-NEB) method[29,30] as implemented in the VASP transition state tools. The effect of van der Waals interactions was taken into account to investigate Li adsorption and diffusion by using the semi-empirical long-range dispersion correction (the PBE-D2 functional),[31] which is essential to account for the long-range electrostatic interactions between Li atoms at high concentrations.[32–34]

Results and discussion

Geometric structure

The optimized crystal structure of the new 3D graphene monolith proposed in this work is presented in Fig. 1a, which is constructed by integrating zigzag graphene nanoribbons with tetrahedrally coordinated carbon chains as cross-linkers. This structure possesses a hexagonal primitive cell containing 42 carbon atoms. Hence, we refer to it as a hexagonal zigzag graphene monolith (HZGM), named HZGM-42. In this primitive cell, there are four chemically nonequivalent carbon atoms: 6g (0, 0.47, 0.25), 12j (0.08, 0.46, 0.25), 12j (0.12, 0.45, 0.75), and 12j (0.20, 0.45, 0.75). The 6g atoms form an sp^3-hybridized carbon chain, whereas the remaining sp^2-hybridized carbons form the zigzag graphene nanoribbons. Owing to its unique porous configuration, HZGM-42 has a low density of 1.39 g cm^{-3}, close to that of nanotube bundles (1.33 g cm^{-3}),[35] and lower than that of fullerene solid (1.65 g cm^{-3}).[18] We also calculated the equilibrium density for some other 3D carbon crystals for comparison. The results are summarized in Table 1, which shows that HZGM-42 has the lowest equilibrium density among those 3D carbon allotropes. The pores of HZGM-42 could accommodate other atoms or molecules for further functionalization as in the case of 3D carbon-nanotube polymers.[16]

To study the effect of van der Waals (vdW) interaction on the geometry of HZGM-42, we recalculated the lattice parameters with semiempirical vdW correction.[31] For comparison, the calculations for diamond and graphite were also carried out. The results are presented in Table S1 in the ESI.† We find that the lattice parameters with and without the semiempirical vdW

Table 1 The space group, lattice constants, calculated equilibrium density (ρ in g cm^{-3}), and the total energy (E_{tot} in eV per atom) of HZGM-42 and some other 3D carbon allotropes

3D crystal	Space group	Lattice constants (a, b, c)	ρ	E_{tot}
HZGM-42	$P6_3/mcm$	16.82, 16.82, 2.47	1.39	−9.09
Graphite	$P6/mmm$	2.46, 2.46, 7.32	2.24	−9.21
Diamond	$Fd\bar{3}m$	4.34, 4.34, 4.34	3.62	−9.09
T6	$P4_2/mmc$	2.60, 2.60, 6.00	3.06	−8.64
bct-C_4	$I4/mmm$	4.38, 4.38, 2.51	3.42	−8.89
IGN	$Cmcm$	4.33, 4.33, 2.47	2.59	−8.98
bco-C_{16}	$Imma$	7.80, 4.90, 3.26	2.57	−8.82
Hex-C_{18}	$P6_3/mcm$	8.36, 8.36, 2.46	2.41	−8.96

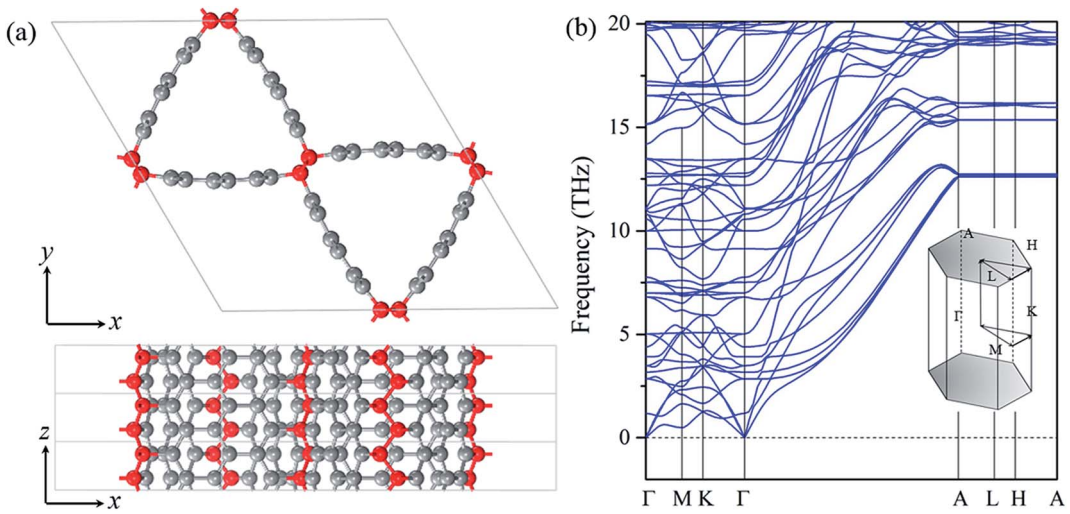

Fig. 1 (a) Top and side views of the optimized geometry structure, and (b) the phonon band structure of HAGM-42. The inset in (b) shows the first Brillouin zone and the high symmetry k point path. The light gray and red spheres represent the sp^2- and sp^3-hybridized carbon atoms, respectively.

correction are almost the same, suggesting that the effect of vdW interaction on the geometry of Hex-C_{18} is weak and negligible due to the strong covalent bonding. Therefore, the following calculations of the thermodynamic and mechanical, and electronic properties of HZGM-42 were carried out using the standard PBE exchange–correlation functional, without vdW corrections.

Energetic stability

To investigate the thermodynamic stability of HZGM-42, we calculated its total energy as a function of volume. For comparison, we also performed calculations of some other 3D carbon crystals, including graphite, diamond, and the recently reported 3D carbon phases, such as T6,[36–38] bct-C_4,[39–41] IGN,[18,42,43] bco-C_{16},[44] and Hex-C_{18}.[45] The results are plotted in Fig. S1.† We find that HZGM-42 possesses satisfactory thermodynamic stability as its total energy per atom is close to that of diamond, the energy difference between HZMG-42 and graphite is only 0.12 eV per atom, and it is energetically favorable over most of the identified 3D metastable carbon phases including T6, bct-C_4, IGN, bco-C_{16}, and Hex-C_{18}. To understand the origin of the high energetic stability of HZMG-42, we analyzed its bonding features. The calculated bond length of the sp^2–sp^2 C–C bond for the nanoribbon motif is in the range of 1.42–1.44 Å. For the sp^3–sp^3 C–C bond in the cross-linkers of sp^3-hybridized carbon chains, the calculated bond length is 1.52 Å. The average bond angle of the sp^2-hybridized carbon atoms is 119.9°, while that of the sp^3-hybridized carbon atoms was 110.0°. The values of bond lengths and angles for the sp^2- and sp^3-hybridized carbon atoms in HZGM-42 are very close to the ideal values of graphite (1.42 Å, 120°) and diamond (1.53 Å, 109.5°), thus leading to the high energetic stability.

Dynamic and thermal stability

To examine the dynamic stability of HZGM-42, we first calculated its phonon band structure. As shown in Fig. 1b, the absence of imaginary modes in the entire Brillouin zone confirms that HZGM-42 is dynamically stable. More interestingly, we note the strong anisotropy of the phonon dispersions. Comparing the acoustic branches and optical branches along the Γ–M and Γ–K paths with those along the Γ–A, the acoustic branches and most of the optical branches along the Γ–A path show respectively larger slopes, indicating that the group velocities of phonons along the z direction are higher than those along the directions inside the xy plane. We then performed the AIMD simulations to verify the thermal stability of HZGM-42 by increasing temperature from 400 K to 1200 K. We used the $1 \times 1 \times 4$ supercell to reduce the constraint associated with periodic boundary conditions. The results of simulation at a temperature of 1200 K are plotted in Fig. S2 in the ESI.† These clearly show that the structural skeleton of HZGM-42 remains almost intact after heating for 8 picoseconds (ps) with a time step of 1 femtosecond (fs), and the average value of the total potential energy remains almost constant during the entire simulation, confirming that HZGM-42 is thermally stable, and can withstand temperatures as high as 1200 K.

Mechanical properties

To study the mechanical properties of HZGM-42, we calculated its elastic constants and Young's moduli, and found that HZGM-42 possesses highly anisotropic mechanical properties due to its unique geometric configuration. The elastic constants (C33) and the Young's modulus of HZGM-42 along the z direction are much larger than those along the x- and y-directions. For comparison, we also calculated the elastic constants and Young's moduli for the recently reported 3D graphene-based architectures, C-honeycomb-28 and C-honeycomb-52 that exhibit superb specific strength along the z direction.[46] The calculated results are given in Table 2. We note that the elastic constants and the Young's modulus along the z direction of HZGM-42 are even larger than the values of C-honeycomb-28 and C-honeycomb-52, indicating that HZGM-42 possesses an ultrahigh specific strength along the z direction.

To gain a further understanding of the mechanical strength of HZGM-42, we also calculated the ideal tensile strength, *i.e.* the maximum stress required for breaking a perfect crystal.[47] In the calculations of the ideal tensile strength, the quasi-static displacement-controlled deformation is used by imposing the deformation with a small strain increment (a typical value of 0.01 is used) along different directions. The stress–strain curves of HZGM-42, C-honeycomb-28, and C-honeycomb-52 subjected to the tensile stresses along the x, y and z directions are displayed in Fig. 2. In contrast to the nonlinear stress–strain response of C-honeycomb-28 and C-honeycomb-52 along the x and y directions, HZGM-42 exhibits a nearly linear stress–strain response along two directions when the strain is less than 0.15, indicating that HZGM-42 is more resistant to tensile stress than C-honeycomb-28 and -52 at the initial strained stage. This linear elasticity of HZMG-42 under tensile loading along the x and y directions is a result of the strongly coupled tension and small bending deformation of the components of zigzag graphene nanoribbons. The ideal tensile strength of HZGM-42 along the z direction is 71.9 GPa, which is higher than the values of C-honeycomb-28 (70.3 GPa) and C-honeycomb-52 (40.1 GPa), confirming its high specific strength along the z direction. The high specific strength of HZGM-42 along the z direction is attributed to the high in-plane strength of the zigzag graphene

Table 2 Calculated elastic constants (C_{ij} in GPa), Young's moduli ($Y_{x/y/z}$ in GPa), and ideal tensile strengths ($T_{x/y/z}$ in GPa) of the 3D graphene monoliths including HZGM-42, C-honeycomb-28, and C-honeycomb-52

	HZGM-42	C-honeycomb-28	C-honeycomb-52
C_{11}	198.0	163.2	95.1
C_{33}	637.7	581.3	365.0
C_{44}	138.4	100.0	67.7
C_{12}	86.5	152.4	92.7
C_{13}	56.3	38.5	32.3
Y_x	240.4	20.8	4.7
Y_y	240.4	20.8	4.7
Y_z	646.7	571.9	353.9
T_x	30.6	37.8	17.2
T_y	20.5	38.6	23.4
T_z	71.9	70.3	41.0

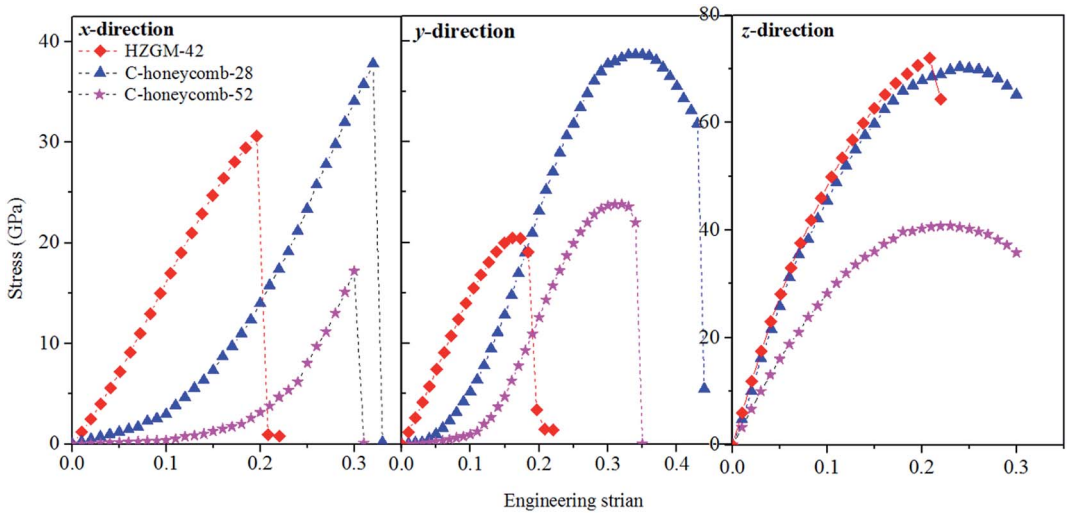

Fig. 2 Orientation-dependent stress–strain relationships for the tensile deformations of HZGM-42, C-honeycomb-28, and C-honeycomb-52.

nanoribbons in the 3D graphene monolith, which is reminiscent of the 3D graphene monoliths assembled by zigzag graphene nanoribbons with high specific strength along the extended direction of zigzag graphene motifs reported by Jiang *et al.*[18]

Electronic properties

To probe the electronic properties of HZGM-42, we calculated its band structure using the PBE functional. As shown in Fig. 3a, HZGM-42 is a semimetal with a Dirac linear dispersion and zero density of states (DOS) near the Fermi level, inheriting the unique electronic properties of graphene. The valence and conduction bands along the high symmetry K path Γ–A belong to two different irreducible representations B_1 and B_2, as shown in Fig. 3a, resulting in the unavoidable band crossing. The irreducible representation of an energy state describes the symmetries of its wave vector and wave function under symmetry operations subject to a certain point group. We calculated the charge density of states at the points (P1 and P2) close to the crossing point, as shown in Fig. S3a,† because the square modulus of the wave function is proportional to the charge density. The difference of the charge density distributions of the two states, as shown in Fig. S3b and c,† which confirms our conclusion that the two bands belong to two different irreducible representations. The band crossing point is located exactly at the Fermi level and is protected by the coexistence of time reversal and space inversion symmetries in HZGM-42 in the absence of the spin–orbit coupling (SOC). Detailed illustration of the relationship between the band crossing point and time reversal and space inversion symmetries is given in Text S1, Fig. S4 and S5 in the ESI.† To confirm the results obtained by the PBE functional, the band structure of HZGM-42 was recalculated using the HSE06 functional, which is known to provide a more accurate band structure as the electron Coulomb screening is more accurately treated in the exchange–correlation energy of electrons in solids.[24] The results plotted in Fig. S6 in the ESI† show that the semimetallic feature of HZGM-42 is well preserved at the HSE06 level, suggesting that semimetallicity is the intrinsic property of HZGM-42.

The partial DOS projected onto the sp^2- and sp^3-hybridized carbon atoms are also displayed in Fig. 3a. It reveals that the dominant contribution to the DOS around the Fermi level comes from the sp^2-hybridized carbon atoms. To further understand the origin of semimetallicity in this new phase, the band-decomposed charge density is calculated to visualize

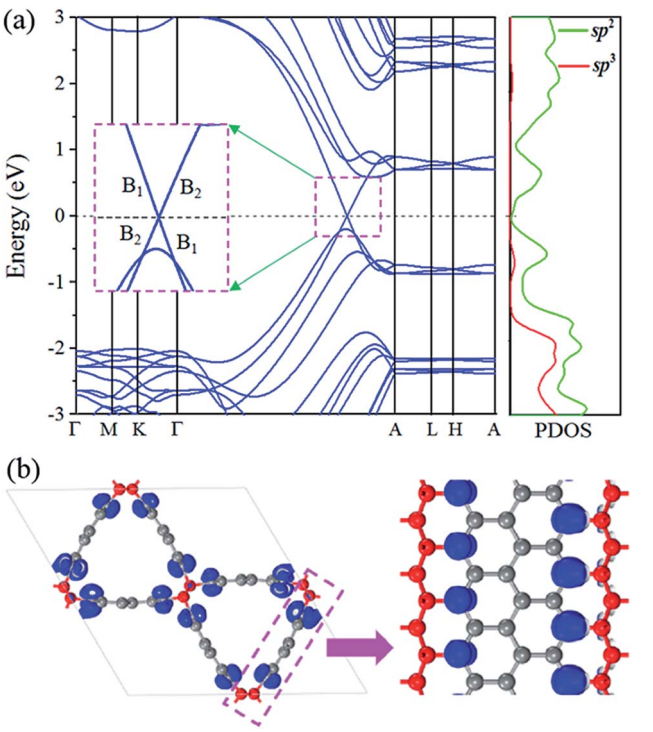

Fig. 3 (a) Electronic band structure and projected DOS of the sp^2-hybridized and sp^3-hybridized carbon atoms. (b) Charge density isosurface (0.04 e Å^{-3}) of the valence bands and conduction bands near the Fermi level.

the charge distribution in the bands near the Fermi level, *i.e.* the 79th to 90th bands including the six occupied bands and six unoccupied bands. As displayed in Fig. 3b, we find that the main contribution to the charge distribution comes from the sp^2-hybridized carbon atoms, which are bound to the sp^3-hybridized carbon chains.

A further analysis of the band structure of HZGM-42 in the whole Brillouin zone indicates that the band crossing points of the valence and conduction bands form nodal-lines traversing the Brillouin zone. Fig. 4 shows the 3D band structure and band gap contour of HZGM-42 in the mirror invariant planes (100) and (110). One can see that the valence and conduction bands cross along the continuous nodal-lines for both planes, characterizing HZGM-42 as a Dirac nodal-line semimetal. However, a band gap may be opened up at the band crossing points by considering SOC for semi-metallic carbon structures.[44] For the case of HZGM-42, the band gap opened up by the SOC is calculated to be 1.23 meV, which is negligibly weak, suggesting that the semi-metallicity of HZGM-42 is not altered by the SOC.[44] To elucidate the topological feature of HZGM-42, we calculated its Z_2 indices following a commonly used method to identify the topology of Dirac nodal-line states.[48–50] The parities at the eight time-reversal invariant momenta (TRIM) points were −1 (Γ), −1 (3 × M), 1 (A), and 1 (3 × L), respectively. Then, we obtained the Z_2 indices as (0; 0 0 0), indicating the topological trivial nature of HZGM-42.

Although HZGM-42 is topologically trivial, its Dirac nodal-line band structure provides great promise for high-speed electronic devices. Due to its unique configuration, HZGM-42 exhibits highly anisotropic electrical transport properties. The extended direction of the sp^3 zigzag chains for HZGM-42 in the real space (z direction) corresponds to the Γ–A direction in the reciprocal space. As shown in Fig. 3a, the electronic bands near the Fermi level along the Γ–A direction exhibit large dispersion, indicating that the carriers moving along the z direction have small effective masses. The carrier velocity can be calculated by using the formula $\overrightarrow{v}_{\vec{k}} = \hbar\frac{d\varepsilon_{\vec{k}}}{d\vec{k}}$ ($\varepsilon_{\vec{k}}$ is the energy and $\vec{k}$ is the wavevector). As a benchmark, we first calculated the velocity of Dirac electrons in graphite. The calculated result of 0.87×10^6 m s^{-1} was in good agreement with the value 0.86×10^6 m s^{-1} obtained by Liu *et al.*,[41] confirming the validity of our calculations. Based on the band structure obtained at the PBE level, the highest carrier velocity of HZGM-42 along the z direction was calculated to be 0.82×10^6 m s^{-1}, which was comparable to the calculated value of Dirac electrons in graphene (0.87×10^6 m s^{-1}). However, the electronic bands along the paths of A–L, L–H, and A–H in the Brillouin zone are much flatter than those along the Γ–A path, suggesting that carriers move much slower in the xy plane than that along the z direction. The highly anisotropic transport properties of HZGM-42 may have potential applications in direction-dependent microelectronic devices.[51]

Application as an anode material for LIBs

Due to its regular porosity and intrinsic semi-metallicity, HZGM-42 can provide the basis for the storage and transport of Li ions with good conductivity, making it possible to use it as an anode material for LIBs. Hence, we systematically studied its binding and diffusion behavior, theoretical capacity, and cycling stability.

We first investigated the binding of a single Li atom into HZGM-42. To avoid the interaction between Li atoms, we adopted a 1 × 1 × 4 supercell. Four possible adsorption sites for the Li atom with high geometric symmetry were considered, marked as Li_I, Li_{II}, Li_{III}, and Li_{IV} in Fig. 5. Li_I is the triangle hollow site, Li_{II} is the center site of the "groove" formed by the 8-membered carbon rings, Li_{III} is the site on the top of the 6-membered carbon rings, and Li_{VI} is the edge site of the "groove" formed by the 8-membered carbon rings. To check the strength

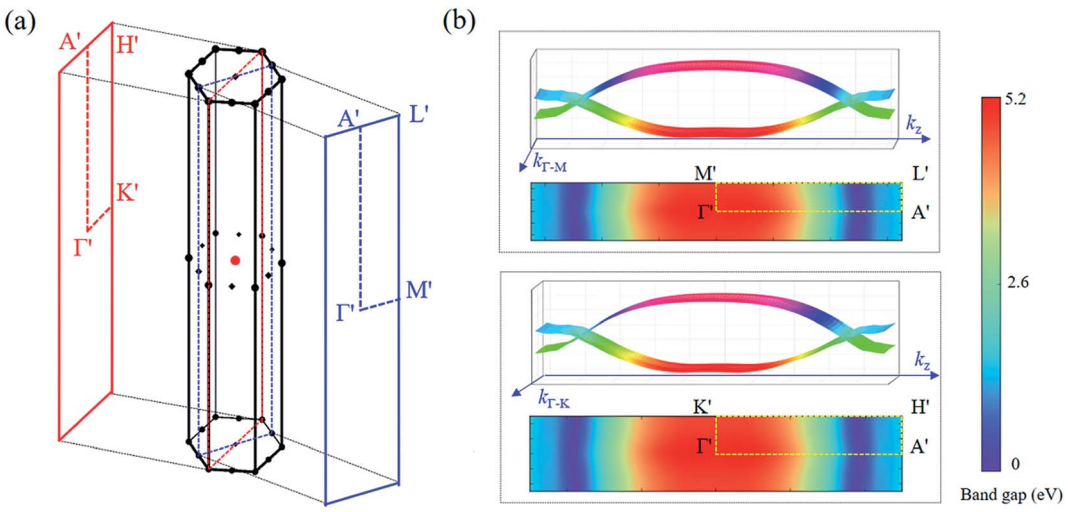

Fig. 4 (a) Bulk Brillouin zone of HZGM-42 with mirror invariant planes (100) indicated by the blue rectangle and (110) indicated by the red rectangle, respectively. (b) 3D band structure (VB and CB) and band gap contour of the two mirror invariant planes. The color bar indicates the band gap at each k point.

of Li binding on the four stable sites, we calculated the Li binding energy (E_b), which is defined as

$$E_b = (E_{Li_x\text{-HZGM-42}} - E_{HZGM\text{-}42} - x\mu_{Li})/x, \quad (1)$$

where $E_{Li_x\text{-HZGM-42}}/E_{HZGM\text{-}42}$ is the total energy of the system with/without Li, and μ_{Li} is the energy of one Li atom in the Li bulk.[34] After full optimizations, Li_I, Li_{II}, and Li_{III} were found to be the stable adsorption sites with the binding energies of −0.89, −0.66, and −0.39 eV, respectively, indicating that the most favorable adsorption site for the Li atom is the triangular hollow site. Li_{IV} was optimized to Li_{II}. The Bader charge analysis[52] revealed that each Li atom transfers 0.89 electrons to the neighboring C atoms when Li is adsorbed onto the Li_I site. For Li_{II} and Li_{III} sites, the transferred charges were found to be 0.88 and 0.90 electrons, respectively. The electron transfer suggests that all the Li atoms in these three adsorption sites donate most of their valence electrons and become Li ions, leading to a strong Coulomb repulsion between the adsorbed Li ions, thus preventing them from clustering.

We next calculated the energy barrier for Li ion diffusion. Because the energy barrier for the Li atom to diffuse through the six-membered carbon rings reaches up to 10 eV,[53] the diffusion along the *xy* plane in HZGM-42 is, thus, kinetically prohibited. Therefore, we here only considered diffusion paths along the *z* direction. Considering the structural symmetry of HZGM-42 and the preferable Li binding sites, we selected two representative diffusion pathways, as shown in Fig. 5c. Path I is along the *z* direction of the triangular hollow channel, while path II is along the *z* direction of the hexagonal hollow channel. Based on climbing-image nudge elastic band (CI-NEB) calculations,[29] the energy profiles along paths I and II are calculated and displayed in Fig. 5d. The calculated diffusion barriers for paths I and II are 0.02 and 0.18 eV, respectively. Both of these are much lower than the diffusion barrier of Li-ions in graphite (0.22–0.40 eV),[54,55] indicating that Li ions can easily diffuse along the two channels. The remarkable 1D Li-ion diffusion paths with low diffusion barriers suggest that HZGM-42 possesses high-rate capability as an anode material for LIBs. To investigate the effect of the point defect on the 1D diffusion barriers in HZGM-42, we created a mono-vacancy at the sp^3 carbon site in the 1 × 1 × 4 supercell (see Fig. S7†), and calculated the symmetry-inequivalent migration paths along the *z* direction around the defect, as displayed in Fig. S8.† We find that for the migration paths in the hexagonal hollow channel, the diffusion barriers of paths A and B are 0.49 eV and 0.23 eV, respectively, which are larger than the value of path II (0.18 eV) in the defect-free structure. For the migration path in the triangular hollow channel, the diffusion barrier increases dramatically from 0.02 eV (path I) to 0.26 eV (path C) when introducing the mono-vacancy of an sp^3 carbon atom, suggesting that the defect can create a potential trap in the defective region, making the diffusion unfavorable. Therefore, it is necessary to avoid the formation of defects in HZGM-42 when used as an anode material in LIBs. Actually, defects can also trap the metal ion even in layered materials.

We next studied the maximum Li capacity of HZGM-42 by increasing the Li concentration until the full Li-intercalated configuration is reached, as shown in Fig. S9 in the ESI.† According to our definition of the binding energy in eqn (1), a more negative binding energy means a more favorable exothermic reaction between Li and HZGM-42. The corresponding average binding energy E_b was calculated to be −0.19 eV, which is larger than that of Hex-C_{18} (−0.42 eV),[45] but lower than that of the $Ti_3C_2(OH)_2$ monolayer ($TiS_3C_2(OH)_2Li_{0.5}$: −0.14 eV)[33] calculated at the same level. This suggests that Li atoms adsorbed onto HZGM-42 are stable, and the phase separation problem is safely avoided at such a high Li concentration. The corresponding theoretical specific capacity of HZGM-42 is 637.71 mA h g^{-1}, which is 1.7 times larger than that of graphite, and larger than the values of recently predicted 3D carbon allotropes, such as bco-C_{16},[4] hex-C_{18},[45] and IGN.[56]

Open-circuit voltage (OCV) is one of the key factors to characterize battery performance under different conditions. It varies with the Li concentration. In general electrode testing,

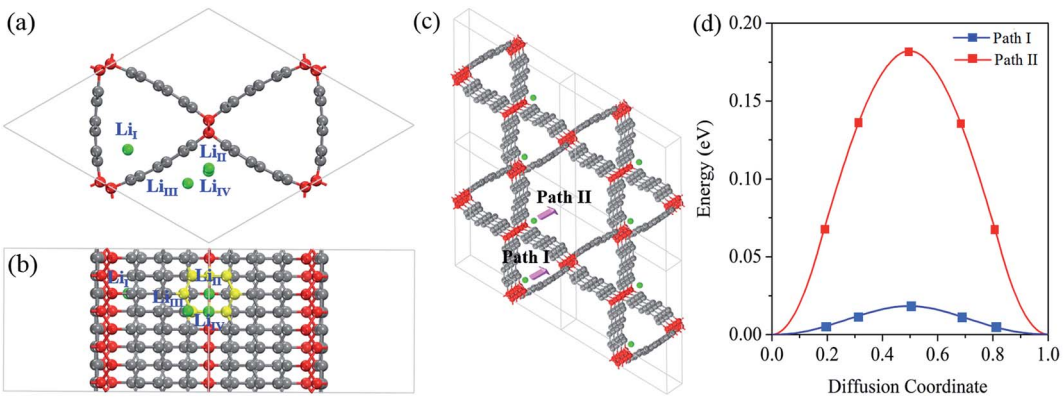

Fig. 5 (a) Top and (b) side views of the possible Li-ion adsorption sites. The green, light gray, and red spheres represent Li, sp^2-, and sp^3-hybridized carbon atoms, respectively. The 8-membered carbon ring is marked in yellow. (c) Two migration paths of Li diffusion considered along the *z* direction in the triangular hollow channel and the hexagonal hollow channel, respectively. (d) The diffusion energy barrier profiles of the two diffusion paths given in (c).

the charge/discharge process of HZGM-42 follows the common half-cell reaction *versus* Li/Li^+:

$$(x_1 - x_2)Li^+ + (x_2 - x_1)e^- + Li_{x_1}\text{-HZGM-42} \leftrightarrow Li_{x_2}\text{-HZGM-42}. \quad (2)$$

Without considering the effects of volume, pressure, and entropy, the average voltage of Li_x-HZGM-42 in the concentration range of $x_1 < x < x_2$ can be estimated using the following formula:

$$V \approx \frac{E_{Li_{x_1}\text{-HZGM-42}} - E_{Li_{x_2}\text{-HZGM-42}} + (x_2 - x_1)E_{Li}}{(x_2 - x_1)}, \quad (3)$$

where $E_{Li_{x_1}\text{-HZGM-42}}$, $E_{Li_{x_2}\text{-HZGM-42}}$, and E_{Li} are the total energy of Li_{x_1}-HZGM-42, Li_{x_2}-HZGM-42, and Li in its bulk phase, respectively.

To calculate $E_{Li_x\text{-HZGM-42}}$, we examined 20 symmetry-inequivalent adsorption configurations and selected the one with the lowest binding energy for each Li concentration ($Li_xC_{3.5}$: x = 0.17, 0.33, 0.50, 0.67, and 0.83). The calculated results are plotted in Fig. 6a. The corresponding voltage profile is further calculated and displayed in Fig. 6b. One can see that there are three prominent voltage regions: the plateau region corresponding to a weak interaction between Li ions at the low Li concentration ($0 < x < 0.50$), the plateau region with increasing repulsive interaction at the medium Li concentration ($0.50 < x < 0.83$), and the region with strong repulsive interaction between Li ions at high Li concentration ($0.83 < x < 1.00$). The voltage profile decreases to −0.12 V when the Li concentration increases to 0.67, suggesting that the reversible capacity of HZGM-42 as the half-cell is 425.14 mA h g^{-1} ($LiC_{5.25}$), which is 66.7% of the maximum Li capacity, larger than those of graphite (372 mA h g^{-1}) and IGN (298 mA h g^{-1}).[56] By numerically averaging the voltage profile in the region of $0 < x < 0.67$, the average voltage of HZGM-42 is calculated to be 0.50 V that is larger than those of graphite (0.11 V)[32] and bco-C_{16} (0.23 V),[4] but smaller than those of IGN,[56] MoC_2,[57] 2D VS_2 (0.93)[32] and TiO_2 (1.5–1.8).[58,59] Note: the above results are all based on the half-cell reaction. When connected to the cathode as a full-cell, the external voltage can overcome the repulsive interaction between Li ions at high concentration, and display a high capacity ($LiC_{3.5}$: 637.71 mA h g^{-1}) and a low average voltage of 0.19 V.

We also assessed the cycling stability of HZGM-42, which is mainly determined by the volume changes during the Li charging/discharging process. We compared the fully Li-intercalated HZGM-42 with the pristine structure, and found that no bond-breaking occurs and the lattice changes along the x, y and z directions are only 0.3%, 0.2%, and 2.0%, respectively. These changes are far less than the fracture strains shown in Fig. 2, confirming that HZGM-42 retains its structural stability during lithiation/delithiation processes. With the small lattice changes, we obtained the total volume expansion to be as low as 2.4%, which is much smaller than that of graphite (10%).[4] The ultra-low volume expansion can be attributed to the nanoporous nature of HZGM-42 that provides sufficient void space for Li-ion insertion. The low volume expansion of Li insertion and the large fracture strain imply that HZGM-42 has a good cycling stability during the lithiation/delithiation process when used as an anode material.

In addition, we found that a series of 3D graphene monoliths with different pore sizes can be generated by changing the width of the zigzag graphene nanoribbons. For instance, another hexagonal zigzag graphene monolith (HZGM) with the same lattice symmetry as that of HZGM-42, containing 66 carbon atoms per primitive cell, called HZGM-66, was constructed. Its dynamic, thermal and mechanical stabilities were confirmed by following the same procedure (see Fig. S10 and S11 in the ESI for details†). HZGM-66 is also a semimetal with a Dirac linear dispersion near the Fermi level, as shown in Fig. S11e.† Therefore, we further explored its potential for LIB anode materials. The calculated diffusion barriers for similar paths (paths I and path II, as shown in Fig. S12†) are 0.03 and 0.17 eV, respectively, close to those of HZGM-42. The maximum

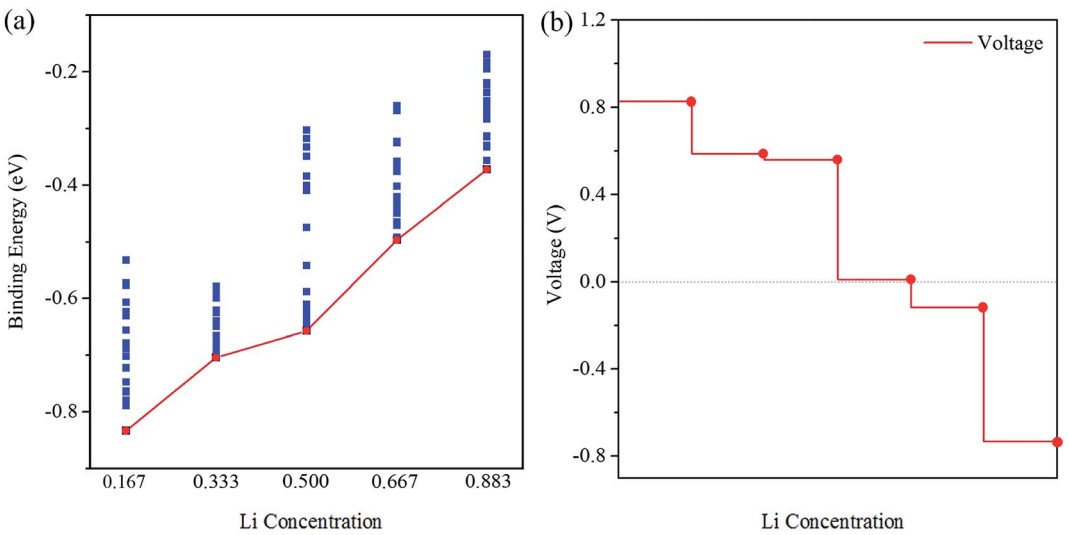

Fig. 6 (a) Binding energies of the 100 configurations for five different Li concentrations. The stable configurations with the lowest energies for each Li concentration are marked in red. (b) The corresponding voltage profile.

Li capacity is 676.36 mA h g^{-1}, which is even larger than that of HZGM-42 (637.71 mA h g^{-1}). The volume expansion is 3.0% for the fully Li-intercalated structure (see Fig. S13†), suggesting a good cycling stability of HZMG-66.

Conclusions

In summary, we predicted a new 3D graphene monolith, HZGM-42, by integrating zigzag graphene nanoribbons with sp^3-hybridized carbon chains as linkers. This material has the advantages of intrinsic high electrical conductivity and ordered porosity for Li-ion transport. By performing state-of-the-art theoretical calculations, we demonstrated that HZGM-42 is not only dynamically, thermally and mechanically stable, but also energetically more favorable than most of the previously identified 3D carbon allotropes. Because of its unique atomic configuration, HZGM-42 exhibits exceptional properties including anisotropic elasticity, high specific ideal strength along the *z* direction, intrinsic Dirac nodal-line semimetallicity and anisotropic transport properties. Moreover, we examined the energetics and kinetics of Li-ion insertion and diffusion in HZGM-42, and the following conclusions can be drawn: (i) Li ions can be inserted into HZGM-42 stably without clustering; (ii) HZGM-42 possesses two remarkable 1D Li-ion diffusion paths and the migration energy barriers can reach quite low values, especially for path I (0.02 eV). (iii) The maximum Li capacity of HZGM-42 is 637.71 mA h g^{-1}, corresponding to $LiC_{3.5}$, which is much higher than that of the commercially used graphite anode (372 mA h g^{-1}; LiC_6). (iv) Compared with the conventional graphite anode, HZGM-42 exhibits a much lower volume change (2.4%) during the Li insertion/removal process, indicating a good cycling stability. With all of these extraordinary characteristics, HZGM-42 shows a great potential as a LIB anode material. Our study reveals the great potential of 3D graphene monoliths with intrinsic semi-metallicity and ordered pores to be applied as LIB anode materials. We hope that these findings will motivate further theoretical and experimental efforts to find new semi-metallic 3D graphene monoliths for high-performance LIB anode materials. These results suggest that, compared to the currently used anode materials in LIBs, the new 3D graphene architecture exhibits superior properties.

Conflicts of interest

The authors declare no competing financial interests.

Acknowledgements

This work is partially supported by grants from the National Key Research and Development Program of China (2016YFE0127300 and 2017YFA0205003) and the National Natural Science Foundation of China (NSFC-51471004 and NSFC-21773004), and also supported by the High Performance Computing Platform of Peking University, China. P. J. acknowledges support by the U.S. Department of Energy, Office of Basic Energy Sciences, Division of Materials Sciences and Engineering under Award #DE-FG02-96ER45579. The authors thank the crew of the Center for Computational Materials Science, the Institute for Materials Research, Tohoku University (Japan), for their continuous support of the HITACHI SR11000 supercomputing facility.

References

1 S. Y. Hong, Y. Kim, Y. Park, A. Choi, N.-S. Choi and K. T. Lee, *Energy Environ. Sci.*, 2013, **6**, 2067–2081.
2 E. M. Erickson, C. Ghanty and D. Aurbach, *J. Phys. Chem. Lett.*, 2014, **5**, 3313–3324.
3 P. G. Bruce, S. A. Freunberger, L. J. Hardwick and J.-M. Tarascon, *Nat. Mater.*, 2012, **11**, 19–29.
4 J. Liu, S. Wang and Q. Sun, *Proc. Natl. Acad. Sci. U. S. A.*, 2017, 201618051.
5 S. Goriparti, E. Miele, F. De Angelis, E. Di Fabrizio, R. P. Zaccaria and C. Capiglia, *J. Power Sources*, 2014, **257**, 421–443.
6 H. Li and H. Zhou, *Chem. Commun.*, 2012, **48**, 1201–1217.
7 L. Ji, Z. Lin, M. Alcoutlabi and X. Zhang, *Energy Environ. Sci.*, 2011, **4**, 2682–2699.
8 C. J. Meyers, S. D. Shah, S. C. Patel, R. M. Sneeringer, C. A. Bessel, N. R. Dollahon, R. A. Leising and E. S. Takeuchi, *J. Phys. Chem. B*, 2001, **105**, 2143–2152.
9 F. Cheng, Z. Tao, J. Liang and J. Chen, *Chem. Mater.*, 2007, **20**, 667–681.
10 A. D. Roberts, X. Li and H. Zhang, *Chem. Soc. Rev.*, 2014, **43**, 4341–4356.
11 X. Deng, B. Zhao, Y. Sha, Y. Zhu, X. Xu and Z. Shao, *ChemElectroChem*, 2016, **3**, 698–703.
12 V. Etacheri, C. Wang, M. J. O'Connell, C. K. Chan and V. G. Pol, *J. Mater. Chem. A*, 2015, **3**, 9861–9868.
13 J. Hou, C. Cao, F. Idrees and X. Ma, *ACS Nano*, 2015, **9**, 2556–2564.
14 K. Umemoto, S. Saito, S. Berber and D. Tománek, *Phys. Rev. B: Condens. Matter Mater. Phys.*, 2001, **64**, 193409.
15 T. Kawai, S. Okada, Y. Miyamoto and A. Oshiyama, *Phys. Rev. B: Condens. Matter Mater. Phys.*, 2005, **72**, 035428.
16 Z. Zhao, B. Xu, L.-M. Wang, X.-F. Zhou, J. He, Z. Liu, H.-T. Wang and Y. Tian, *ACS Nano*, 2011, **5**, 7226–7234.
17 Z. Zhu, Z. G. Fthenakis, J. Guan and D. Tománek, *Phys. Rev. Lett.*, 2014, **112**, 026803.
18 X. Jiang, J. Zhao, Y. L. Li and R. Ahuja, *Adv. Funct. Mater.*, 2013, **23**, 5846–5853.
19 N. V. Krainyukova and E. N. Zubarev, *Phys. Rev. Lett.*, 2016, **116**, 055501.
20 Y. Gao, Y. Chen, C. Zhong, Z. Zhang, Y. Xie and S. Zhang, *Nanoscale*, 2016, **8**, 12863–12868.
21 G. Kresse and J. Furthmüller, *Phys. Rev. B: Condens. Matter Mater. Phys.*, 1996, **54**, 11169.
22 J. P. Perdew, K. Burke and M. Ernzerhof, *Phys. Rev. Lett.*, 1996, **77**, 3865.
23 P. E. Blöchl, *Phys. Rev. B: Condens. Matter Mater. Phys.*, 1994, **50**, 17953.
24 J. Heyd, G. E. Scuseria and M. Ernzerhof, *J. Chem. Phys.*, 2003, **118**, 8207–8215.

25 H. J. Monkhorst and J. D. Pack, *Phys. Rev. B: Condens. Matter Mater. Phys.*, 1976, **13**, 5188.
26 S. Nosé, *J. Chem. Phys.*, 1984, **81**, 511–519.
27 X. Gonze, *Phys. Rev. B: Condens. Matter Mater. Phys.*, 1997, **55**, 10337–10354.
28 A. Togo, F. Oba and I. Tanaka, *Phys. Rev. B: Condens. Matter Mater. Phys.*, 2008, **78**, 134106.
29 G. Henkelman, B. P. Uberuaga and H. Jónsson, *J. Chem. Phys.*, 2000, **113**, 9901–9904.
30 G. Henkelman and H. Jónsson, *J. Chem. Phys.*, 2000, **113**, 9978–9985.
31 S. Grimme, *J. Comput. Chem.*, 2006, **27**, 1787–1799.
32 Y. Jing, Z. Zhou, C. R. Cabrera and Z. Chen, *J. Phys. Chem. C*, 2013, **117**, 25409–25413.
33 Q. Tang, Z. Zhou and P. Shen, *J. Am. Chem. Soc.*, 2012, **134**, 16909–16916.
34 E. Lee and K. A. Persson, *Nano Lett.*, 2012, **12**, 4624–4628.
35 S. Yamanaka, A. Kubo, K. Inumaru, K. Komaguchi, N. Kini, T. Inoue and T. Irifune, *Phys. Rev. Lett.*, 2006, **96**, 076602.
36 K. M. Merz Jr, R. Hoffmann and A. T. Balaban, *J. Am. Chem. Soc.*, 1987, **109**, 6742–6751.
37 M. J. Bucknum and R. Hoffmann, *J. Am. Chem. Soc.*, 1994, **116**, 11456–11464.
38 S. Zhang, Q. Wang, X. Chen and P. Jena, *Proc. Natl. Acad. Sci. U. S. A.*, 2013, **110**, 18809–18813.
39 K. Umemoto, R. M. Wentzcovitch, S. Saito and T. Miyake, *Phys. Rev. Lett.*, 2010, **104**, 125504.
40 P. A. Schultz, K. Leung and E. Stechel, *Phys. Rev. B: Condens. Matter Mater. Phys.*, 1999, **59**, 733.
41 Y. Liu, X. Jiang, J. Fu and J. Zhao, *Carbon*, 2018, **126**, 601–610.
42 Y. Chen, Y. Xie, S. A. Yang, H. Pan, F. Zhang, M. L. Cohen and S. Zhang, *Nano Lett.*, 2015, **15**, 6974–6978.
43 V. A. Blatov and D. M. Proserpio, *Acta Crystallogr., Sect. A: Found. Crystallogr.*, 2009, **65**, 202–212.
44 J.-T. Wang, H. Weng, S. Nie, Z. Fang, Y. Kawazoe and C. Chen, *Phys. Rev. Lett.*, 2016, **116**, 195501.
45 J. Liu, T. Zhao, S. Zhang and Q. Wang, *Nano Energy*, 2017, **38**, 263–270.
46 Z. Pang, X. Gu, Y. Wei, R. Yang and M. S. Dresselhaus, *Nano Lett.*, 2016, **17**, 179–185.
47 Y. Zhang, H. Sun and C. Chen, *Phys. Rev. Lett.*, 2004, **93**, 195504.
48 Y. Kim, B. J. Wieder, C. Kane and A. M. Rappe, *Phys. Rev. Lett.*, 2015, **115**, 036806.
49 R. Li, H. Ma, X. Cheng, S. Wang, D. Li, Z. Zhang, Y. Li and X.-Q. Chen, *Phys. Rev. Lett.*, 2016, **117**, 096401.
50 R. Yu, H. Weng, Z. Fang, X. Dai and X. Hu, *Phys. Rev. Lett.*, 2015, **115**, 036807.
51 J. Lahiri, Y. Lin, P. Bozkurt, I. I. Oleynik and M. Batzill, *Nat. Nanotechnol.*, 2010, **5**, 326–329.
52 W. Tang, E. Sanville and G. Henkelman, *J. Phys.: Condens. Matter*, 2009, **21**, 084204.
53 K. Nishidate and M. Hasegawa, *Phys. Rev. B: Condens. Matter Mater. Phys.*, 2005, **71**, 245418.
54 K. Persson, V. A. Sethuraman, L. J. Hardwick, Y. Hinuma, Y. S. Meng, A. van der Ven, V. Srinivasan, R. Kostecki and G. Ceder, *J. Phys. Chem. Lett.*, 2010, **1**, 1176–1180.
55 W. Li, Y. Yang, G. Zhang and Y.-W. Zhang, *Nano Lett.*, 2015, **15**, 1691–1697.
56 J. Liu, S. Wang, Y. Qie, C. Zhang and Q. Sun, *Phys. Rev. Mater.*, 2018, **2**, 025403.
57 D. Çakır, C. Sevik, O. Gülseren and F. M. Peeters, *J. Mater. Chem. A*, 2016, **4**, 6029–6035.
58 M. Aydinol, A. Kohan, G. Ceder, K. Cho and J. Joannopoulos, *Phys. Rev. B: Condens. Matter Mater. Phys.*, 1997, **56**, 1354.
59 Z. Yang, D. Choi, S. Kerisit, K. M. Rosso, D. Wang, J. Zhang, G. Graff and J. Liu, *J. Power Sources*, 2009, **192**, 588–598.